



FPGA-based position reconstruction method for neutron beam flux spatial distribution measurement in BNCT

Wei Jiang^{1,2} · Ping Cao^{1,3} · Yi-Ming Wu^{1,2} · Xian-Ke Liu^{1,3} · Zhu-Jun Fang^{1,2} · Zhi-Yong Zhang^{1,2} · Bin Shi⁴ · Jun Chen⁴

Received: 16 August 2023 / Revised: 7 November 2023 / Accepted: 8 November 2023 / Published online: 3 May 2024

© The Author(s), under exclusive licence to China Science Publishing & Media Ltd. (Science Press), Shanghai Institute of Applied Physics, the Chinese Academy of Sciences, Chinese Nuclear Society 2024

Abstract

A new measurement method for the spatial distribution of neutron beam flux in boron neutron capture therapy (BNCT) is being developed based on the two-dimensional Micromegas detector. To address the issue of long processing times in traditional offline position reconstruction methods, this paper proposes a field programmable gate array based online position reconstruction method utilizing the micro-time projection chamber principle. This method encapsulates key technical aspects: a self-adaptive serial link technique built upon the dynamical adjustment of the delay chain length, fast sorting, a coordinate-matching technique based on the mapping between signal timestamps and random access memory (RAM) addresses, and a precise start point-merging technique utilizing a circular combined RAM. The performance test of the self-adaptive serial link shows that the bit error rate of the link is better than 10^{-12} at a confidence level of 99%, ensuring reliable data transmission. The experiment utilizing the readout electronics and Micromegas detector shows a spatial resolution of approximately 1.4 mm, surpassing the current method's resolution level of 5 mm. The beam experiment confirms that the readout electronics system can obtain the flux spatial distribution of neutron beams online, thus validating the feasibility of the position reconstruction method. The online position reconstruction method avoids traditional methods, such as bubble sorting and traversal searching, simplifies the design of the logic firmware, and reduces the time complexity from $O(n^2)$ to $O(n)$. This study contributes to the advancement in measuring neutron beam flux for BNCT.

Keywords Position reconstruction · FPGA · Readout electronics · Neutron flux spatial distribution

1 Introduction

Boron neutron capture therapy (BNCT) is a progressive radiation therapy technology that selectively eliminates tumors at the cellular level [1, 2]. With the advancements in accelerator-based neutron sources in recent years, BNCT has overcome the previous nuclear safety risk associated with traditional reactor-based neutron sources [3–5]. This progress is increasingly fostering prospects for its clinical application in hospitals. The spatial distribution of neutron beam flux is a critical parameter in the physical and clinical dosimetry of BNCT, because it fundamentally influences the precision of radiation dosage. However, there is currently no internationally standardized measurement method for this parameter. Traditional methods, such as point-by-point scanning with active detectors or the spatial arrangement of passive detectors, suffer from drawbacks such as long measurement times, complex operations, and low accuracy [3–9].

This work was supported by the National Natural Science Foundation of China (No. 12075237).

✉ Ping Cao
cping@ustc.edu.cn

¹ State Key Laboratory of Particle Detection and Electronics, University of Science and Technology of China, Hefei 230026, China

² Department of Modern Physics, University of Science and Technology of China, Hefei 230026, China

³ School of Nuclear Science and Technology, University of Science and Technology of China, Hefei 230026, China

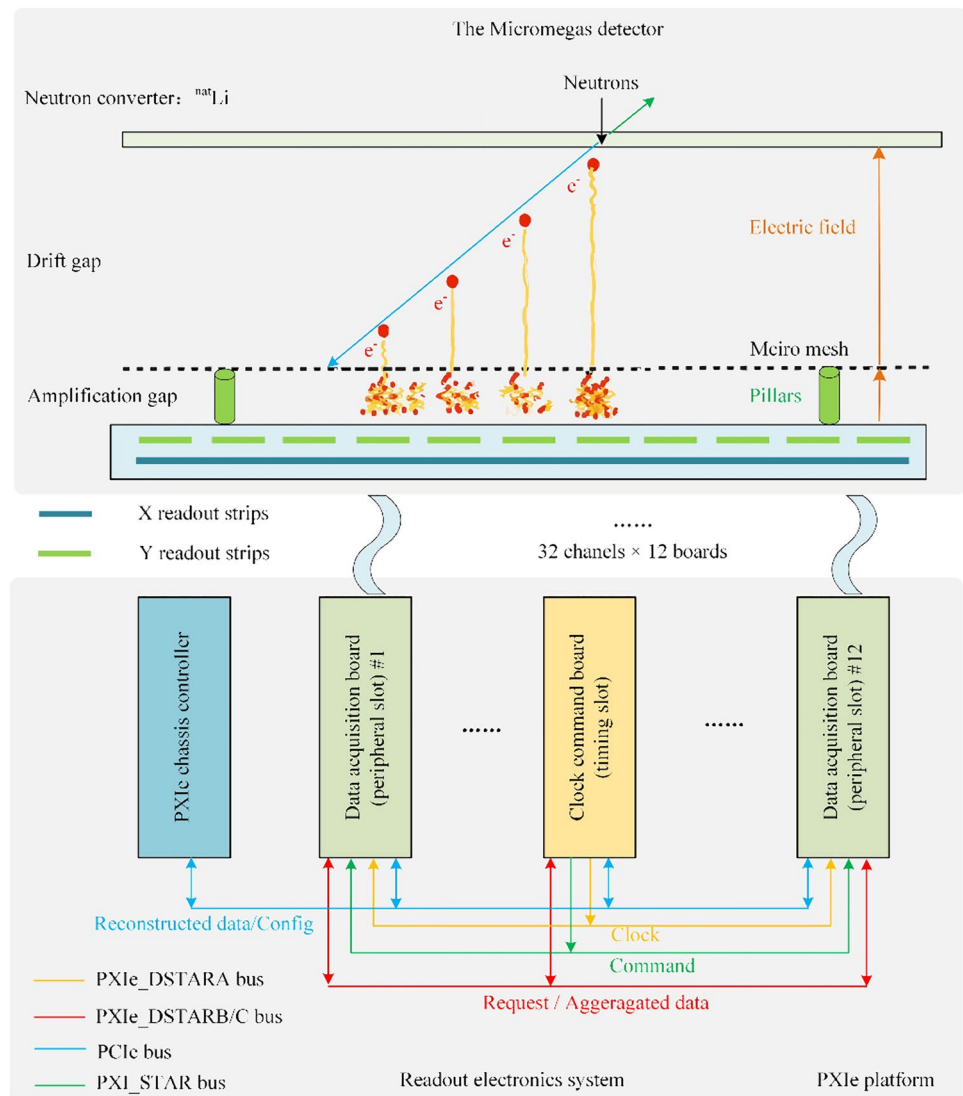
⁴ National Key Laboratory for Metrology and Calibration Techniques, China Institute of Atomic Energy, Beijing 102413, China

The Micromegas (Micro Mesh Gaseous Structure) detector is a two-dimensional micropattern gaseous detector [10]. It offers fast two-dimensional beam imaging via a single measurement [11]. In this study, Micromegas detectors are adopted to measure the spatial distribution of neutron beam flux in BNCT. The measurement system, consisting of the Micromegas detector and readout electronics is depicted in Fig. 1 [12, 13]. The Micromegas detector uses a ^{nat}LiF film as the converter, initially engaging in the ${}^6\text{Li}(n, \alpha){}^3\text{H}$ reaction with neutrons. The resultant charged particles undergo primary ionization and sequential avalanche amplification in the drift and amplification gaps, respectively. Finally, current signals are induced on anode readout strips. The Micromegas detector used is equipped with 192 readout strips in the X-direction and Y-direction. The 384 readout strips are connected to the readout electronics system through several micro-coaxial flat cables. The readout electronics are designed as a modular structure in the PXI Express (PXIe)

platform, including 12 modular data acquisition boards (DABs) and 1 clock command board (CCB) [13]. The DABs amplify, digitize, and shape the current signals from the 384 detector strips. The CCB is located in the system timing slot. It distributes the system clock and the start and stop acquisition commands to 12 DABs via star buses of the chassis backplane.

The rapid acquisition of measurement results is important for improving equipment practicality and measurement efficiency. Although the Micromegas detector is utilized to shorten the data acquisition process, the data analysis process can still be time-consuming. This is because conventional readout electronics systems typically only handle data acquisition, with the collected data being analyzed offline through software [14–18]. Several minutes are normally needed to analyze the large volume of data, which does not meet user requirements. The major time-consuming part of offline software data processing is particle position

Fig. 1 (Color online) Measurement system consists of the micromegas detector and readout electronics



reconstruction. To address the issue, this study utilizes the parallel computing characteristic and real-time capabilities of a field programmable gate array (FPGA) to perform online particle position reconstruction.

Two particle position reconstruction principles are commonly employed when the Micromegas detector is used for particle position measurement: the charge centroid principle and the micro-time projection chamber (μ TPC) principle [19–21]. The charge centroid principle reconstructs the hit position by calculating the average of the strip positions weighted by the strip charge. The μ TPC principle treats the Micromegas detector as a micro-time projection chamber. It combines a group of signals caused by a single incident particle and merges them into the signal with the latest arrival time within the group. The readout strip corresponding to the signal with the latest arrival time is considered as the entry point of the particle [19, 20]. This process is called start point mergence in this study.

Compared with the charge centroid principle, the μ TPC principle has a simpler calculation process if it is implemented in an FPGA. Furthermore, multiple studies have shown that the charge centroid principle is suitable for use in cases in which charged particles are approximately emitted vertically, and its accuracy of position reconstruction rapidly deteriorates as the emission angle increases. By contrast, the μ TPC principle exhibits excellent position reconstruction accuracy across the entire angular range [19, 20]. Secondary charged particles resulting from ${}^6\text{Li}(n, \alpha){}^3\text{H}$ neutron interactions are randomly emitted at a 4π solid angle. According to these considerations, the μ TPC principle is chosen for neutron position reconstruction in this study.

According to the μ TPC principle, the particle position reconstruction involves operations such as data aggregation from multiple DABs, signal time sorting, start point merging, and XY coordinate matching. Due to the high neutron flux, data acquisition only takes a few seconds. After data acquisition is completed, the particle position reconstruction process is initiated, and the reconstructed data are uploaded from the CCB to the chassis controller.

Computational software for general computers often includes well-developed sorting and searching algorithms. However, these algorithms are not suitable for direct porting to FPGAs. On the one hand, an FPGA has limited on-chip memory resources compared with general computers, and its underlying architecture differs from that of a central processing unit. Therefore, the FPGA is not proficient in sorting and searching operations involving large amounts of data. Implementing these software algorithms directly on an FPGA would lead to complex firmware design. On the other hand, the algorithms provided by conventional software often have high time complexity. For instance, typical algorithms such as bubble sorting and traverse search have a time complexity of $O(n^2)$ [22]. If these software algorithms

are directly ported to an FPGA, they may not fully leverage the hardware acceleration advantages of the FPGA.

To sum up, the demand for rapidly obtaining measurement results poses a challenge to the readout electronics system in terms of FPGA-based online particle position reconstruction. This paper will fully utilize the characteristics of the FPGA and propose a hardware-friendly online position reconstruction method.

2 Online hardware position reconstruction method

2.1 Data aggregation built on the self-adaptive serial link technique

The primary step in aggregating data is to establish the transmission link between the DABs and the CCB. The CCB serves as the main site for online position reconstruction. The DABs and the CCB are connected via serial star buses. The clock phase at both ends may vary during different power-on periods, which poses a challenge for stable data transmission over the serial link. To address this issue, this study proposes a self-adaptive serial link by dynamically adjusting the delay chain length. Figure 2a shows the composition of the link.

The data aggregation link works in full-duplex mode. Read requests are transmitted as high level voltage pulses via a PXIe_DSTARB star bus, and the data are aggregated via a PXIe_DSTARC star bus [23]. The output serializer/deserializer (OSERDES) and corresponding input serializer/deserializer (ISERDES) modules in Fig. 2a are used for data serialization and deserialization, respectively [24]. The differential input buffer (IBUFDS) and differential output buffer (OBUFDS) modules are used for single-ended to differential voltage level conversion. Input delay resource (IDELAY) chains are programmable and play a core role in the self-adaptive serial link. They are located on the input path of the FPGA pins, and each includes 64 delay elements [25]. By changing the length of the delay chains at the receiver end, the phase relationship between the data and the clock can be adjusted, ensuring the proper sampling of the data by the clock.

Since this study adopts a strategy of collecting data first and then performing position reconstruction, there is no special requirement for the link rate. This study opts for a clock with a frequency of 62.5 MHz, which is half of the FPGA device clock. Thus, the corresponding serial aggregation link rate is 625 Mbps.

Before the DABs can send parallel data to the CCB, an initialization process is required to establish the connection of the link. The initialization process involves the transmission of handshake signals through the PXI_STAR bus.

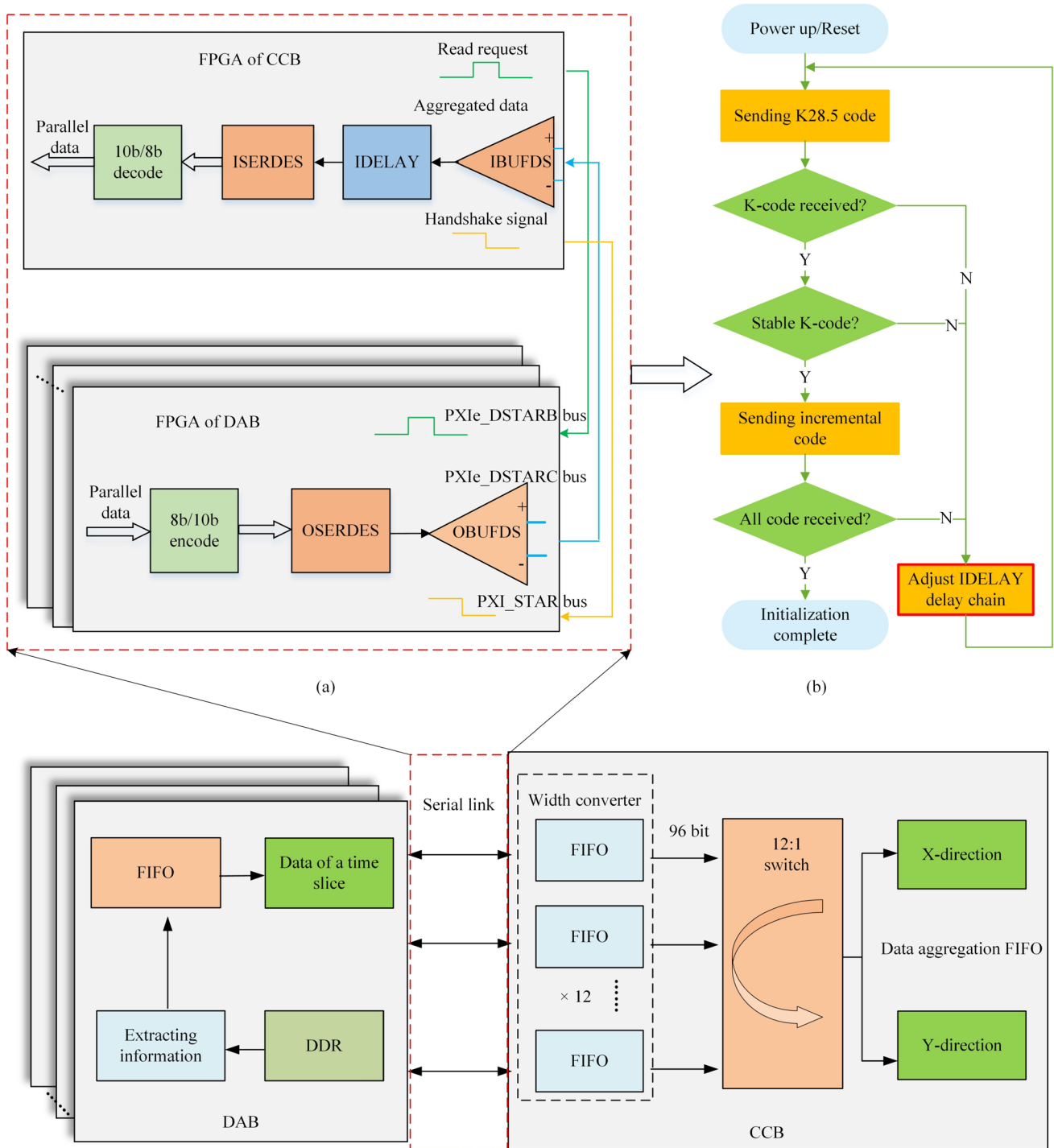


Fig. 2 (Color online) Data aggregation built on the self-adaptive serial link technique. **a** Composition of the data aggregation link. **b** Flowchart of the initialization of the self-adaptive serial link. **c** Data aggregation process between the CCB and DABs

Figure 2b shows the following steps for establishing the connection of the self-adaptive serial link.

- *Step 1* The DAB sends a K28.5 control code stream through the PXIe_DSTARC bus while the CCB keeps the PXI_STAR bus at a low voltage level.
- *Step 2* The CCB utilizes the ISERDES module to detect and locate the boundaries of the serial data

stream for checking the recovery of the K-code. If the CCB fails to recover the K28.5 code, the system proceeds to Step 3; otherwise, it proceeds to Step 4.

- *Step 3* The CCB dynamically adjusts the IDELAY chain length by adding a delay element to the IDELAY chain. Then, the system proceeds to Step 1.
- *Step 4* If a certain number of consecutive K28.5 control codes are received, the system proceeds to Step 5; otherwise, it returns to Step 3.
- *Step 5* The CCB sets the PXI_STAR to a high voltage level, and the DAB sends a sequence of incrementing codes (0×00 to $0 \times FF$). Then, the system proceeds to Step 6. The reason for sending incremental codes from 0×00 to $0 \times FF$ is that the receiving end may be in a metastable state in which it can correctly receive the K28.5 control code but not some other data. The incremental codes help detect whether the receiving end is in a stable state.
- *Step 6* If the incrementing code is correctly received by the CCB, the system proceeds to Step 7; otherwise, it proceeds to Step 3.
- *Step 7* The initialization of the link is complete. The link is now ready for data transmission. The system will continue to transmit the K28.5 control code and keep the PXI_STAR signal high when the link is idle.

To accommodate the limited on-chip storage resources of the FPGA, this study adopts a time slicing approach for data aggregation. The data aggregation process between the CCB and DABs is depicted in Fig. 2c. Once data acquisition is completed, the CCB sends a data read request. Next, each DAB reads the waveform data from the onboard DDR (double data rate) memory, where the waveform data of over-threshold valid signals are preserved in time order. The waveform data are then further processed to extract the signal's amplitude, timestamp, and channel number information, which is next stored in a first-in, first-out (FIFO). The DAB reads the data corresponding to the next time slice from the FIFO and sends them to the CCB. Subsequently, the CCB stores the data from all 12 channels into a width conversion FIFO. This width conversion step ensures that the port transmission capacity of the 12:1 switch is consistent, preventing data congestion during the aggregation process. Finally, the CCB polls the width conversion FIFO to retrieve the data and writes the signal information into two separate FIFOs: one for the *X*-direction and one for the *Y*-direction. After completing the data aggregation of a time slice, the CCB proceeds with subsequent data processing operations. Once finished, it sends a data read request for the next time slice in preparation for the next round of processing.

2.2 Fast sorting and coordinate matching technique based on timestamp to RAM address mapping

Due to independent acquisition among DABs, the data aggregated into the *X*- and *Y*-direction FIFOs are time-disordered. Therefore, this study proposes a fast sorting technique based on the mapping between signal timestamps and random access memory (RAM) addresses, as described in Fig. 3a. The timestamp of a signal is mapped to the address of an FPGA on-chip RAM, and the channel number and amplitude of the signal are the contents of the RAM storage. Figure 3a provides an intuitive understanding, where time-ordered signals on the time axis are rotated by 90 degrees, resulting in a structure that closely resembles that of the RAM.

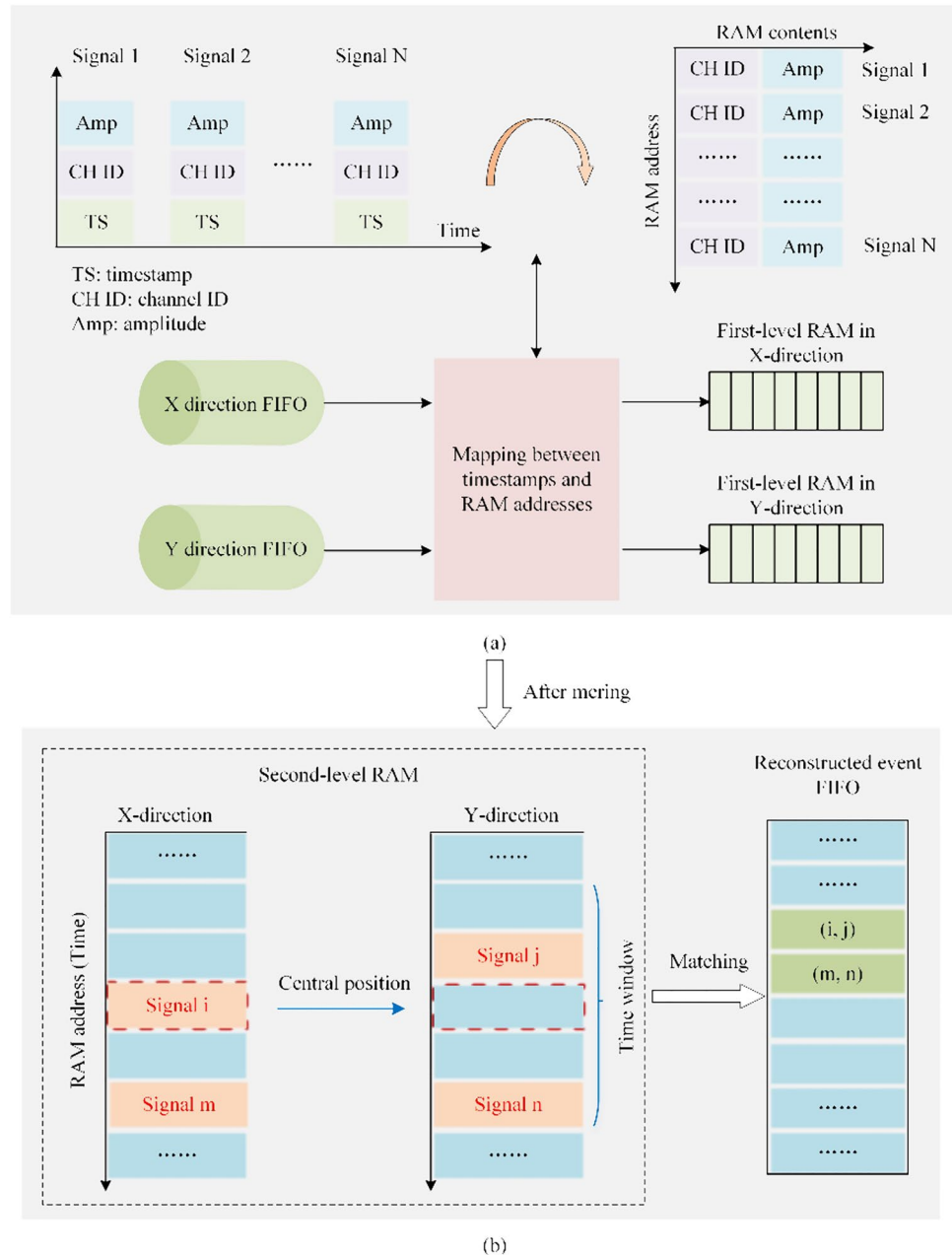
The depth of the RAM which stores the data of a single time slice should be equal to the length of the time slice. The timestamp to RAM address mapping uses the lower *N* bits of the timestamp as the address of the RAM, where *N* and the depth of the RAM (Depth) follow a relationship of $2^N = \text{Depth}$. This allows the *N*-bit timestamp to be directly mapped to the entire circular RAM address. The sorting module writes the data to the first-level RAM based on the mapped address. A RAM address unit corresponds to a timestamp unit of 10 ns, which is the sampling interval of the ADC. Considering FPGA resource utilization, the RAM depth is set to 2048. Hence, the time slice length is 20.48 μs . The probability of two signal timestamps being the same is low, so no other operations are needed to handle this situation.

After sorting and merging processes in the *X*- and *Y*-directions, a further coordinate matching operation is required. Coordinate matching follows two principles: time alignment and nearest matching. Time alignment means that the time difference between the timestamps of the *X*-direction and *Y*-direction signals should be smaller than the predefined time window. Nearest matching means that if two or more signals are found within the time window, the *X* and *Y* direction signals with the closest timestamps are matched.

A typical coordinate matching process proceeds as follows. For each *X*-direction signal, search for the *Y*-direction signal that has the smallest time difference. If the time difference between this pair of *X* and *Y* signals falls within the time window, generate a particle coordinate. Otherwise, the *X*-direction signal is considered as an isolated signal without a matching *Y*-direction signal. Then, continue processing the next *X*-direction signal until all *X* signals have been traversed. For each *X*-direction signal, this coordinate matching process requires a search through the *Y*-direction signals, resulting in a loop traversal operation. Therefore, the overall time complexity of this method is $O(n^2)$.

This study proposes a fast coordinate matching technique based on the previous timestamp to RAM address

Fig. 3 (Color online) Fast sorting and coordinate matching technique based on timestamp to RAM address mapping. **a** Sorting process. **b** Matching process



mapping, as shown in Fig. 3b. The merged signals are stored in the second-level RAM, with addresses still following the timestamp to RAM address mapping relationship. The X-direction and Y-direction signals share the same RAM address reference, which means they are aligned on the time axis. Therefore, when searching for a matching Y-direction signal for each X-direction signal, it is only necessary to expand a range of RAM addresses as wide as the time window in the Y-direction RAM and find the nearest non-empty address within the time window. This address corresponds to the matched Y-direction signal. The coordinate matching for all signals can be completed by traversing through the second-level RAM of the

X-direction. The reconstructed event information is then stored in a FIFO buffer and transmitted to the chassis controller via the peripheral component interconnect express (PCIe) bus.

The fast sorting and coordinate matching technique based on the timestamp to RAM address mapping offers the advantages of low time complexity and simple implementation. On the one hand, this technique avoids complex conventional algorithms such as bubble sort and traversal search. Thus, the time complexity is reduced from $O(n^2)$ to $O(n)$. On the other hand, this technique streamlines sorting and searching into basic RAM read–write operations and is relatively simple to implement on an FPGA.

2.3 Precise start point merging technique utilizing a circular combined RAM

According to the μ TPC principle, after the sorting operation, it is necessary to merge the groups of signals that have close channel numbers and timestamps into the starting signal of each group. When merging the signals at the end of each time slice, their starting signals may exist at the beginning of the next time slice.

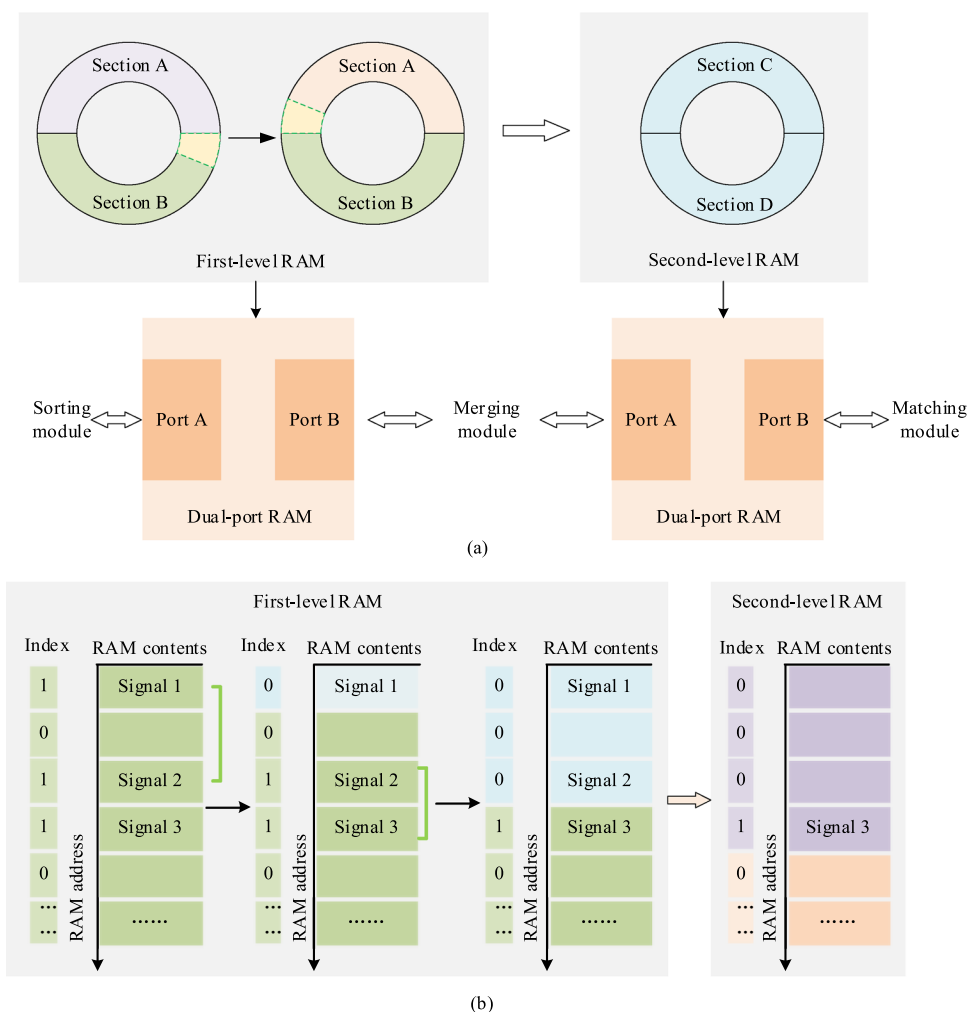
This study designs a circular combined RAM structure to effectively solve this problem, as shown in Fig. 4a. When merging the signals at the tail of one RAM slice, the signals at the head of the other RAM slice can be read to determine whether merging is needed. The merged signals are then written into the second-level RAM for subsequent coordinate matching operations.

RAM is read and written by both the upstream and downstream modules. It is crucial to design a well-coordinated timing relationship to prevent conflicts between RAM read and write operations. To address this issue, dual-port on-chip RAMs are utilized. The read and write operations of

the RAM are coordinated depending on the status signals from the upstream and downstream modules. The explanation below focuses on the first-level RAM involved in the sorting and merging modules, but the same principles also apply to the second-level RAM used in the merging and matching modules.

The first-level circular RAM consists of sections A and B, and each section corresponds to a single time slice. At the initial state when the RAM is empty, the sorting module writes data into sections A and B. It then sends a sorting completion signal to the merging module. After the initial state, every time the sorting module finishes writing a time slice of data into one section of the RAM, it sends a sorting completion signal to the merging module. Upon receiving the sorting completion signal, the merging module performs the merging operation on the other section of the RAM and sends a merging completion signal to the sorting module. It is important to note that the section of the RAM used for merging in each iteration is different from the section where the sorting module was just written. The two sections of RAM are used in a ping-pong-like manner, as depicted in Fig. 4a. This process is repeated to complete

Fig. 4 (Color online) Precise start point merging technique utilizing a circular combined RAM. **a** The circular combined RAM structure for precisely merging signals at the boundary of two time slices. **b** The successive merging process



the merging of signals for all time slices. Furthermore, taking advantage of the parallel computing capabilities of FPGAs, the signal merging operations can be performed simultaneously in both the X -direction and Y -direction. Figure 4 illustrates only one direction of the merging operation, but the same operations are carried out in the other direction, as well.

The number of readout strips hit by charged particles varies, depending on the particle's emission angle. Therefore, it is uncertain how many other signals need to be read when merging each signal. To address this issue, this study adopts a successive merging approach based on the circular combined RAM, as illustrated in Fig. 4b. During the merge of a signal, a time window is opened, starting from this signal and extending toward the later time direction. Within the time window, only the first signal that closely matches the channel number of the current signal is sought. If one such signal is found, there is no need to check for other signals within the time window. The current signal is merged into the later signal, updating its amplitude as the sum of the two and incrementing the merged channel count by one. The amplitude and the merged channel count information could provide support for further event selection. If no candidate is found to be merged within the time window, then the current signal is the starting signal, and the signal is written to the same address in the second-level RAM.

Considering the presence of many empty addresses in RAM, it is necessary to skip these blank addresses to improve data processing efficiency. This applies not only to the merging module but also to the coordinate matching module. To address this, this study adopts a dynamic indexing register to mark whether each address in RAM contains valid data, enabling the blank addresses to be skipped. Taking the first-level RAM shown in Fig. 4 as an example, the bit number of the indexing register is equal to the RAM depth, where each bit corresponds to one address in RAM. During the process of time sorting, if a specific address in RAM is written with data, the corresponding bit in the register is set to 1. While traversing the valid data in RAM to merge signals, the multiple branch selection statement (case \times statement in the Verilog language) is used to quickly locate the first nonzero bit in the indexing register. This corresponds to the first non-empty storage address in RAM. Once the merging of the signal at the corresponding address is completed, the corresponding bit in the indexing register is set to 0. This process is repeated, and as the merging of signals in the entire time slice is completed, all bits in the indexing register are dynamically cleared to zero.

3 Tests and verification

3.1 Self-adaptive serial link test

The self-adaptive serial link is the foundation for position reconstruction. Hence, a test of the reliability of the link is needed. The performance test of the serial link is carried out from two perspectives: eye diagram and bit error rate (BER).

The eye diagram of the digital signal reflects its overall reliability and quality [26]. The test result, as shown in Fig. 5, indicates a clear eye diagram with a wide opening range. The eye width measures approximately 1400 ps, which indicates the excellent quality of the serial link.

A further BER test was carried out to verify whether the method of dynamically adjusting the delay chain length can achieve accurate clock sampling of serial data, thus examining the feasibility of the self-adaptive serial link. In the BER test, the DAB sends a certain number of pseudo-random number sequences while the CCB recovers the pseudo-random numbers and compares them with locally generated pseudo-random numbers in the same mode. Equation (1) shows the relationship between the link error rate and confidence level, according to the hypothesis testing theory in statistics. In the equation, n and k represent the number of bits in the pseudo-random sequence and the number of detected errors, respectively. CL denotes the confidence level at which the link error rate is less than p [27]. The BER test process lasted for approximately 3 h, during which a pseudo-random number sequence of 6.75×10^{12} bits was transmitted with the link rate set to 625 Mbps. No errors were detected in the test procedure. It can be inferred that the BER is less than 10^{-12} at a confidence level of 99%, meeting the reliability standards of conventional high-speed serial links, such as the PCIe bus. This shows that despite the inherent lack of synchronization between the local receiver clock and the incoming serial data stream, the self-adaptive serial link protocol proposed in this study allows the receiver to dynamically adjust the lengths of the programmable delay chains. This automatically fine-tunes the phase relationship between the serial data stream and the clock, ultimately enabling the asynchronous receiver clock to perform precise sampling of the serial data stream. In summary, the experimental results indicate the capability of the self-adaptive serial link to ensure stable and dependable data transmission.

The notable advantages of the self-adaptive serial link lie in the simplicity of physical link connections and the ability to easily implement link protocols using common FPGA logic resources. Consequently, this addresses a constraint encountered in our study, namely, the quantity limitation of backplane buses on the PXIe platform. By

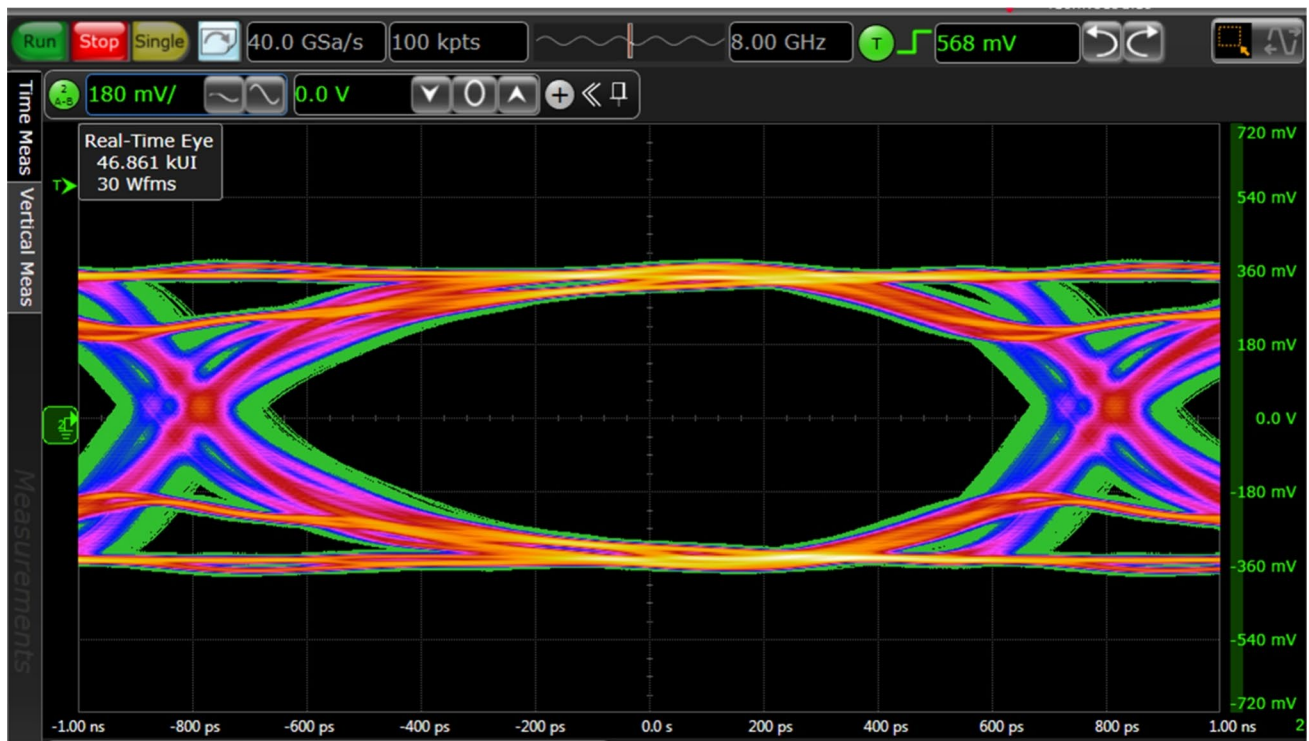


Fig. 5 Eye diagram of the self-adaptive serial link

contrast, conventional synchronous parallel transmission methods necessitate dedicated clock signal paths and multiple parallel data links at both the transmitter and receiver ends. Further, traditional high-speed serial transmission methods based on gigabit transceivers (GT) consume the scarce GT core resources of an FPGA, making them unsuitable for aggregating data across a dozen or more circuit boards.

$$CL = 1 - \sum_{m=0}^k \frac{\lambda^m}{m!} e^{-\lambda}, (\lambda = np) \tag{1}$$

3.2 Position resolution experiment

The position resolution experiment was conducted with a standard Am-Be neutron source and a known semi-circular ⁶LiF conversion film affixed to the Micromegas detector. Due to the relatively low intensity of the Am-Be neutron source, in this particular experiment, a thick (2 μm) pure ⁶LiF conversion film was utilized. The imaging result of the Am-Be neutron radiation field is shown in Fig. 6a. The spatial resolution of the system can be estimated by fitting the neutron count distribution at the semi-circle's diameter boundary. The image is further rotated by 45°, and neutron counts are accumulated along the diameter boundary of the semicircle.

The experimental distribution $B(x')$ of the accumulated hits at the semicircle's diameter boundary is the convolution of the actual particle distribution $T(x)$ and the system's Gaussian response function $R(x, x')$, as shown in Eq. (2) and Eq. (3) [28, 29]. Positional resolution tests for micropattern gas detectors typically employ specific shaping components to adjust the spatial distribution $T(x)$ of particles entering the detector into the expected distribution. Since neutrons are electrically neutral, the conversion film itself can serve as the shaping component. Narrow slits or blades are the most commonly used shaping components because the expected distributions of neutrons passing through them are simple δ and step distributions, respectively. For simplicity in the experiment, an existing circular conversion film was divided into two halves, and the diameter of a semicircle could be regarded as a blade. Consequently, the actual distribution of incident particles at the diameter conforms to a step distribution. Furthermore, the experimental distribution $B(x')$ is simplified as a cumulative Gaussian distribution, as shown in Eq. (4). By fitting the experimental data as shown in Fig. 6b, the standard deviation (σ) of the fit can be obtained, which indicates a spatial resolution of approximately 1.4 mm. As mentioned in the introduction, conventional measurement methods mainly rely on point-by-point scanning with active detectors or a spatial arrangement of passive detectors. The accuracy of these methods is approximately 5

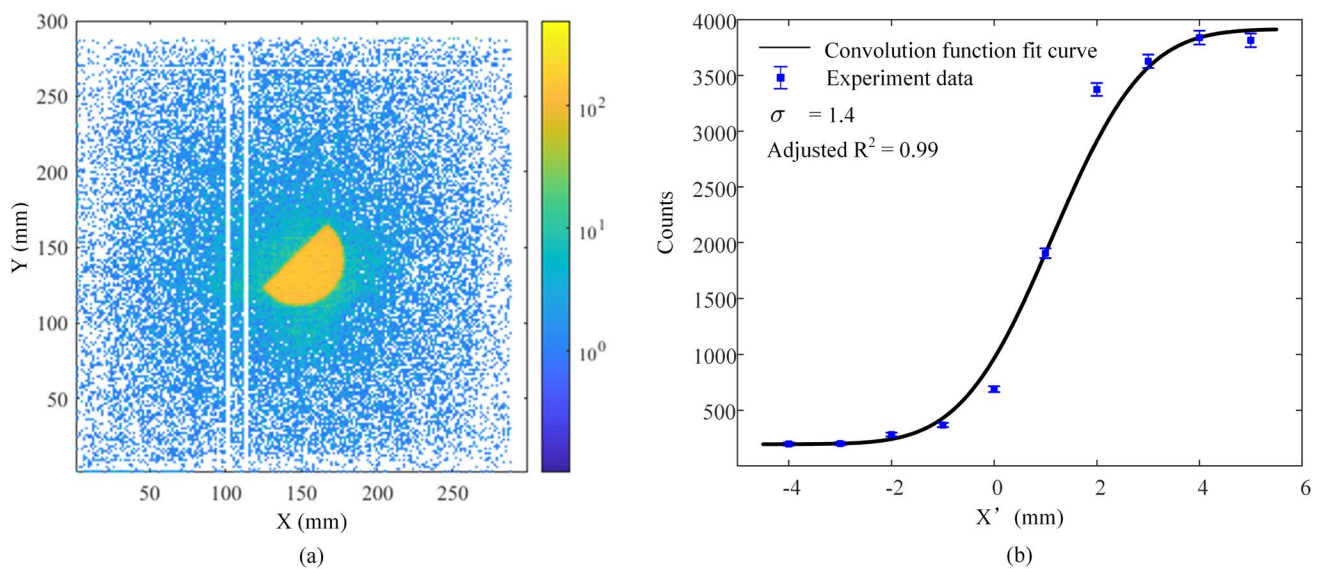


Fig. 6 (Color online) Experimental results of position resolution. **a** Imaging result of the Am-Be neutron radiation field. **b** Fitting result with the convolution function of the step and Gaussian distributions

mm to 1 cm [30–33]. In comparison, the method proposed in this study improves the measurement accuracy to 1.4 mm.

$$B(x') = \int_{-\infty}^{+\infty} T(x) \cdot R(x, x') dx \quad (2)$$

$$R(x, x') = \frac{1}{\sqrt{2\pi}\sigma} \exp\left[-\frac{(x - x')^2}{2\sigma^2}\right] \quad (3)$$

$$B(x') = \int_{x_{\min}}^{x'} R(x) dx \quad (4)$$

The high spatial resolution exhibited in the experiment results mainly arises from two key factors. Primarily, this study employs a Micromegas micropattern detector with a pitch of only 1.5-mm between the readout strips. According to the principles of the uniform distribution, it can be inferred that the strip pitch determines the theoretical limit of the system's spatial resolution to be approximately 0.43 mm (standard deviation). Moreover, the FPGA-based hardware position reconstruction algorithm proposed in this paper is founded on the μ TPC principle. As discussed in the introduction, the μ TPC principle takes the Micromegas detector as a micro-time-projection chamber to enable the reconstruction of the starting point of the particle's initial ionization drift path through the temporal order of multiple induced signals. Previous research has indicated that the

μ TPC principle offers superior position reconstruction accuracy compared with traditional centroid methods [19, 20].

3.3 BNCT beam experiment

The beam experiment was conducted on a dedicated BNCT reactor neutron source, namely, the in-hospital neutron irradiator at the China Institute of Atomic Energy. The theoretical flux of the neutron beam is up to 10^9 n cm⁻²·s⁻¹ [34]. Considering the high beam flux, an ultra-thin (30 nm) conversion film was employed in the experiment, and natural LiF, rather than purified ⁶LiF, was adopted as the conversion material to minimize conversion efficiency. Figure 7a displays a photograph of the experimental setup, and Fig. 7b shows the spatial distribution of thermal neutron components in the beam obtained with the conversion film.

It can be observed that the profile of the neutron beam exhibits a circular profile with a diameter of approximately 12 cm, which conforms to the shape of the beam outlet. The evenly distributed light-colored grid points result from the mesh pillars of the Micromegas detector. The spacing between the mesh pillars is approximately 10 mm, and the diameter is approximately 1 mm, which is consistent with the measurement results. The large-area ^{nat}LiF film for the thermal neutron detector is composed of four 10 cm × 10 cm square films. Therefore, the slightly lower neutron counts at the junction of the ^{nat}LiF films and the 20 cm × 20 cm square boundary outside the beam profile can be seen.

During the beam test, the position reconstruction results are obtained immediately after data acquisition is completed. Compared to the measurement times of hours for traditional

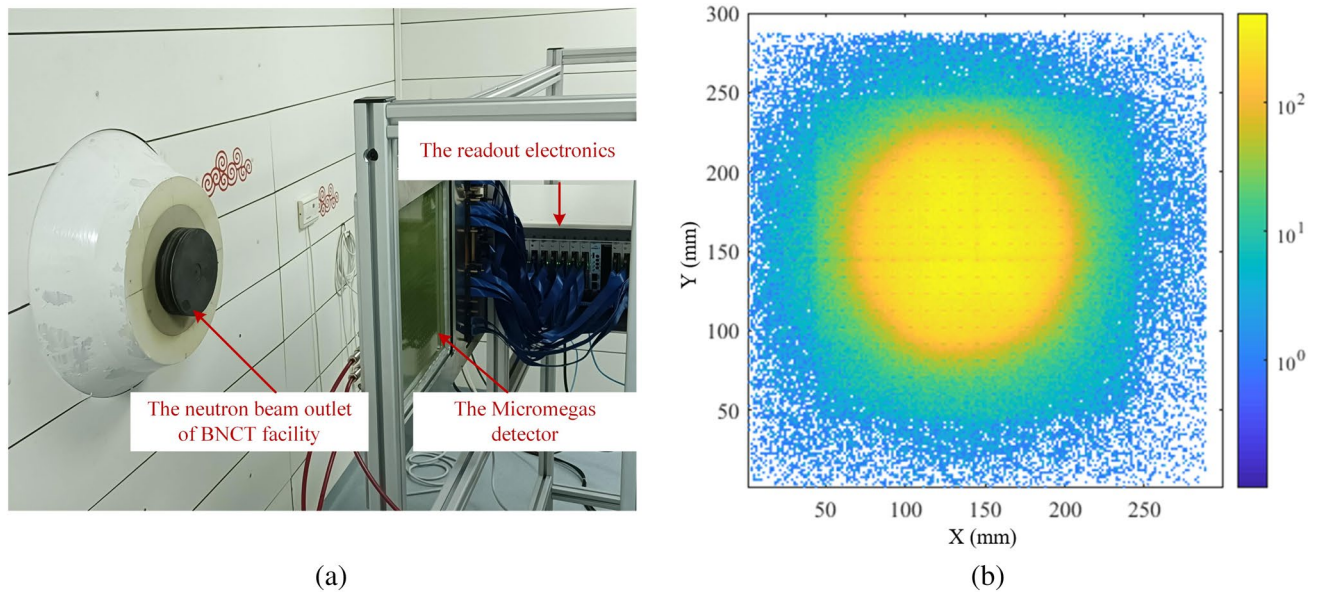


Fig. 7 (Color online) **a** Photograph of the neutron beam experiment. **b** Spatial distribution of thermal neutrons obtained with the ^{nat}LiF conversion film

point-by-point scanning with active detectors or a spatial arrangement of passive detectors, this study improves the equipment's practicality and measurement efficiency.

Additionally, the spatial distribution of the neutron beam flux in BNCT is concerned with the relative distribution rather than the absolute value of the neutron flux. This parameter will serve as a relative coefficient input into the future BNCT treatment planning system. Thus, practical numerical values are not presented here. If accurate absolute fluence values for specific points can be measured in the future, in conjunction with the spatial distribution measurement method demonstrated in this paper for relative fluence, a complete two-dimensional absolute fluence distribution can be obtained. Moreover, due to the challenge of producing a large, uniformly ultra-thin (30 nm) ^{nat}LiF film, preliminary tests were conducted using four 10 cm \times 10 cm square films pieced together. Uniformity calibration of the films was not performed in the preliminary tests, making it difficult to obtain comprehensive and precise uniformity values of the beam flux at this stage. The nuclear reactor is normally shut down, and the availability of beam time for experiments is limited. Therefore, these limitations will be addressed further in future system-level work.

In summary, although there are some imperfections in the test results, the preliminary beam experiment has confirmed the online rapid measurement capability of the FPGA-based particle position reconstruction method proposed in this paper. Furthermore, the details of the beam experiment results, along with the results of the position resolution experiment, indicate the system's excellent spatial resolution.

4 Conclusion

This paper proposes an FPGA-based online position reconstruction method, rooted in the μTPC principle, that effectively eliminates the need for lengthy offline data processing, thereby enhancing equipment practicality and improving measurement efficiency. This study contributes to advancing the application of Micromegas detectors in measuring the flux spatial distributions of BNCT neutron beams, consequently forming a rapid and precise measurement technique. In response to the difficulty faced by FPGAs in sorting and searching operations, this study presents a rapid sorting and searching technique based on timestamp to RAM address mapping. In comparison to traditional approaches such as bubble sorting and traversal searching, the proposed method simplifies the design of logic firmware and reduces time complexity from $O(n^2)$ to $O(n)$. In addition, given the prevalence of timestamps as common pieces of information in physics experiments, the proposed method can provide valuable insights and references for researchers who need to execute timestamp-related algorithms within an FPGA.

Author contributions All authors contributed to the study conception and design. Material preparation, data collection, and analysis were performed by Wei Jiang, Ping Cao, Yi-Ming Wu, Xian-Ke Liu, Zhu-Jun Fang, Zhi-Yong Zhang, Bin Shi, and Jun Chen. The first draft of the manuscript was written by Wei Jiang, and all authors commented on previous versions of the manuscript. All authors read and approved the final manuscript.

Data availability The data that support the findings of this study are openly available in Science Data Bank at <https://cstr.cn/31253.11.scien>

cedb.j00186.00173 and <https://doi.org/10.57760/sciencedb.j00186.00173>.

Declarations

Conflict of interest The authors declare that they have no conflict of interests.

References

- M.A. Dymova, S.Y. Taskaev, V.A. Richter et al., Boron neutron capture therapy: current status and future perspectives. *Cancer Commun.* **40**, 406–421 (2020). <https://doi.org/10.1002/cac2.12089>
- M. Suzuki, Boron neutron capture therapy (BNCT): a unique role in radiotherapy with a view to entering the accelerator-based BNCT era. *Int. J. Clin. Oncol.* **25**, 43–50 (2020). <https://doi.org/10.1007/s10147-019-01480-4>
- J.Y. Chen, J.F. Tong, Z.L. Hu et al., Evaluation of neutron beam characteristics for D-BNCT01 facility. *Nucl. Sci. Tech.* **33**, 12 (2022). <https://doi.org/10.1007/s41365-022-00996-1>
- Y. Lu, W.Y. Li, Z. Xu et al., Experimental terminal design of BNCT neutron source based on 14 MeV proton cyclotron. *Nucl. Tech.* **45**, 030202 (2022). [https://doi.org/10.11889/j.0253-3219.2022.hjs.45.030202\(inChinese\)](https://doi.org/10.11889/j.0253-3219.2022.hjs.45.030202(inChinese))
- Z.Q. Guo, C.Q. Liu, W.Z. Zhang et al., Optimization design of BNCT neutron source and moderating body based on accelerator ${}^7\text{Li}(p, n)$ reaction. *Nucl. Tech.* **45**, 050201 (2022). [https://doi.org/10.11889/j.0253-3219.2022.hjs.45.050201\(inChinese\)](https://doi.org/10.11889/j.0253-3219.2022.hjs.45.050201(inChinese))
- K. Hirose, T. Kato, T. Harada et al., Determining a methodology of dosimetric quality assurance for commercially available accelerator-based boron neutron capture therapy system. *J. Radiat. Res.* **63**, 620–635 (2022). <https://doi.org/10.1093/jrr/rrac030>
- R.D. Rogus, O.K. Harling, J.C. Yanch, Mixed field dosimetry of epithermal neutron beams for boron neutron-capture therapy at the mitr-ii research reactor. *Med. Phys.* **21**, 1611–1625 (1994). <https://doi.org/10.1118/1.597267>
- T.T. Nguyen, T. Kajimoto, K. Tanaka et al., Triple ionization chamber method for clinical dose monitoring with a Be-covered Li BNCT field. *Med. Phys.* **43**, 6050–6057 (2016). <https://doi.org/10.1118/1.4963222>
- Y. Sakurai, H. Tanaka, T. Takata et al., Advances in boron neutron capture therapy (BNCT) at kyoto university - from reactor-based BNCT to accelerator-based BNCT. *J. Korean Phys. Soc.* **67**, 76–81 (2015). <https://doi.org/10.3938/jkps.67.76>
- Y. Giomataris, P. Rebourgeard, J.P. Robert et al., MICROMEAS: A high-granularity position-sensitive gaseous detector for high particle-flux environments. *Nucl. Instrum. Meth. A.* **376**, 29–35 (1996). [https://doi.org/10.1016/0168-9002\(96\)00175-1](https://doi.org/10.1016/0168-9002(96)00175-1)
- D. Attié, S. Aune, E. Berthoumieux et al., Current status and future developments of Micromegas detectors for physics and applications. *Appl. Sci.* **11**, 5362 (2021). <https://doi.org/10.3390/app1125362>
- Z.J. Fang, Z.Y. Zhang, B. Shi et al., A large area, high counting rate micromegas-based neutron detector for BNCT. *Nucl. Instrum. Meth. A.* **1053**, 168361 (2023). <https://doi.org/10.1016/j.nima.2023.168361>
- W. Jiang, P. Cao, X. Liu et al., Readout electronics for spatial distribution measurement of neutron beam flux in BNCT. *J. Instrum.* **18**, P06034 (2023). <https://doi.org/10.1088/1748-0221/18/06/P06034>
- B.B. Qi, Y. Li, D.Y. Zhu et al., Measurement of the neutron beam profile of the Back-n white neutron facility at CSNS with a Micromegas detector. *Nucl. Instrum. Meth. A.* **957**, 163407 (2020). doi:<https://doi.org/10.1016/j.nima.2020.163407>
- T. Alexopoulos, D. Attié, R. Avramidou et al., Study of a micromegas chamber in a neutron beam. *J. Instrum.* **5**, P2005 (2010). <https://doi.org/10.1088/1748-0221/5/02/P02005>
- Y.J. Li, F. Li, S. Zhou et al., Design of the readout electronics system with high event rate based on the Micromegas Detector. *Nucl. Instrum. Meth. A.* **1052**, 168254 (2023). <https://doi.org/10.1016/j.nima.2023.168254>
- Z. Zhang, X. Wang, P. Miao et al., Design of the readout electronics for a Micromegas-TPC detector. *J. Instrum.* **15**, T8007 (2020). <https://doi.org/10.1088/1748-0221/15/08/T8007>
- L. Yu, P. Cao, J.W. Li et al., Multiplexing readout method based on switch arrays for position sensitive thermal neutron detectors. *J. Instrum.* **13**, P11011 (2018). <https://doi.org/10.1088/1748-0221/13/11/P11011>
- T. Alexopoulos, M. Bianco, M. Biglietti et al., Performance studies of resistive-strip bulk micromegas detectors in view of the ATLAS New Small Wheel upgrade. *Nucl. Instrum. Meth. A.* **937**, 125–140 (2019). <https://doi.org/10.1016/j.nima.2019.04.050>
- F. Kuger, Performance studies of resistive Micromegas detectors for the upgrade of the ATLAS Muon spectrometer. *Nucl. Instrum. Meth. A.* **845**, 248–252 (2017). <https://doi.org/10.1016/j.nima.2016.06.006>
- L. Lavezzi, M. Alexeev, A. Amoroso et al., Standalone codes for simulation and reconstruction of a triple-GEM: GTS and GRAAL. *J. Phys. Conf. Ser.* **1561**, 012014 (2020). <https://doi.org/10.1088/1742-6596/1561/1/012014>
- S. Buradagunta, J.D. Bodapati, N.B. Mundukur et al., Performance comparison of sorting algorithms with random numbers as inputs. *Ingénierie Des Systèmes D Inf.* **25**, 113–117 (2020). <https://doi.org/10.18280/isi.250115>
- NI, PXIe-1085 specifications, <https://www.ni.com/docs/zh-CN/bundle/pxie-1085-specs/page/specs.html>. Accessed 14 Aug 2023
- Xilinx, LVDS source synchronous 7:1 serialization and deserialization using clock multiplication application note, <https://docs.xilinx.com/v/u/en-US/xapp585-lvds-source-synch-serdes-clock-multiplication>. Accessed 14 Aug 2023
- Xilinx, 7 series FPGAs selectIO resources user guide, https://docs.xilinx.com/v/u/en-US/ug471_7Series_SelectIO. Accessed 14 Aug 2023
- M.A. Kossel, M.L. Schmatz, Jitter measurements of high-speed serial links. *IEEE Des. Test Comput.* **21**, 536–543 (2004). <https://doi.org/10.1109/MDT.2004.93>
- M. Rice, B. Mazzeo, On the superiority of the negative binomial test over the binomial test for estimating the bit error rate. *IEEE Trans. Commun.* **60**, 2971–2981 (2012). <https://doi.org/10.1109/TCOMM.2012.072612.110495>
- X.Y. Lü, R.R. Fan, Y.B. Chen et al., Study of measuring methods on spatial resolution of a GEM imaging detector. *Chin. Phys. C* **36**, 228 (2012). <https://doi.org/10.1088/1674-1137/36/3/007>
- R.S. Wang, Y. Huang, Z.G. Xiao et al., A practical method to determine the spatial resolution of GEM detector. *Nucl. Instrum. Meth. A.* **701**, 54–57 (2013). <https://doi.org/10.1016/j.nima.2012.10.078>
- P.E. Tsai, Y.H. Liu, H.M. Liu et al., Characterization of a BNCT beam using neutron activation and indirect neutron radiography. *Radiat. Meas.* **45**, 1167–1170 (2010). <https://doi.org/10.1016/j.radmeas.2010.07.008>
- T. Kobayashi, Y. Sakurai, M. Ishikawa, A noninvasive dose estimation system for clinical BNCT based on PG-SPECT - Conceptual study and fundamental experiments using HPGe and CdTe semiconductor detectors. *Med. Phys.* **27**, 2124–2132 (2000). <https://doi.org/10.1118/1.1288243>
- P.E. Tsai, Y.H. Liu, C.K. Huang et al., Neutron flux mapping inside a cubic and a head PMMA phantom using indirect neutron

- radiography. *Appl. Radiat. Isot.* **67**, S190–S194 (2009). <https://doi.org/10.1016/j.apradiso.2009.03.047>
33. Y. Kasesaz, H. Khalafi, F. Rahmani et al., A feasibility study of the Tehran research reactor as a neutron source for BNCT. *Appl. Radiat. Isot.* **90**, 132–137 (2014). <https://doi.org/10.1016/j.apradiso.2014.03.028>
34. J. Chen, C.J. Li, W. Li et al., Neutron spectra measurement of IHNI-I BNCT beam with multi-sphere spectrometer. *At. Energy Sci. Technol.* **48**, 2127–2132 (2014). (in Chinese)

Springer Nature or its licensor (e.g. a society or other partner) holds exclusive rights to this article under a publishing agreement with the author(s) or other rightsholder(s); author self-archiving of the accepted manuscript version of this article is solely governed by the terms of such publishing agreement and applicable law.